Highlights

Pushing and pulling an algal bloom: Physical controls of diel variability in nearshore phytoplankton biomass

Medea Zanoli, Gotzon Basterretxea, Idan Tuval

- Nearshore phytoplankton assemblages can undergo fast short-term variations not exclusively imputable to population growth.
- These diel changes in microalgal cell abundance are the source of enhanced water discoloration and other harmful effects.
- Wind and buoyancy-driven flows were identified as key drivers of the observed fluctuations in Palma Beach (NW Mediterranean).
- A 1D advection-diffusion model successfully diagnoses the mechanisms underlying the daily dynamics of the proliferation of coastal microalgae.

Pushing and pulling an algal bloom: Physical controls of diel variability in nearshore phytoplankton biomass

Medea Zanoli, Gotzon Basterretxea, Idan Tuval[a,*]

[a]*Mediterranean Institute of Advanced Studies IMEDEA (UIB-CSIC), Carrer Miquel Marques 21, Esporles, 07190, Spain*

Abstract

High-biomass microalgal blooms frequently occur in littoral environments worldwide, often causing noxious effects on aquatic ecosystems and coastal communities. Here, we combine field observations and a simple retention-dispersion model to disentangle the short-term ($\sim$ hours) environmental drivers shaping the nearshore dynamics of such outbreaks. Temperature, salinity, fluorescence, current velocities, and meteorological variables were measured in the nearshore waters of a coastal location in Mallorca (Balearic Islands) during the summer of 2018. Daily averages from field data were used to adjust wind and buoyancy flow variations into a one-dimensional advection-diffusion model in the cross-shore direction. Results reveal that the interplay between wind forcing and cross-shore density gradients drives an alternating retention dispersion mechanism, effectively explaining the observed diel chlorophyll variability within the nearshore boundary. This simplified model captures the primary dynamics of the bloom, isolating key factors that

*Corresponding author; email ituval@imedea.uib-csic.es

influence its behavior and offering practical insights for coastal water quality monitoring and management.

Keywords: Phytoplankton, Chlorophyll, Wind stress, Thermo-haline flow, Advection - diffusion model, Ground water, Littoral dynamics

1. Introduction

Phytoplankton are key unicellular organisms that thrive in fresh and ocean waters, playing a vital role in the production of organic matter and oxygen, while also contributing to the regulation of global CO_2 levels and the Earth's climate. However, under favorable environmental conditions, phytoplankton can multiply and accumulate, causing negative effects on the ecological balance of aquatic ecosystems. These high biomass Harmful Algal Blooms (HABs) cause significant socio-economic impacts on local communities and, in some cases, toxicity effects may arise [1] [2].

Phytoplankton and, particularly some species of microalgae, often find suitable environments to proliferate in coastal waters, where enclosed areas like estuaries and bays offer suitable conditions for calm waters with high nutrient availability from terrestrial inputs [3]. In more exposed locations, coastal HABs may occur as massive cell accumulations extending along a nearshore stripe producing a perceivable cross-shore gradient in water discoloration [4].

Phytoplankton growth in the coastal boundary is favored by terrestrial nutrient sources delivered to nearshore waters by rivers, urban outlets, or submarine groundwater discharges (SGD), which introduce an abundance of nutrients that are otherwise scarce in seawater[5] [6]. The prime force driving circulation in the coastal boundary zone is the wind; however, the effects of stratification produced by terrestrial seeps and warming during the summer

period can become very important [7] [8]. The diurnal sea breeze, which on many coasts is seasonal and locally predictable in its occurrence, represents a recurrent force affecting the cross-shore distribution of material and organisms suspended in the water column [9]. Also, fresh and brackish water discharges in the nearshore and diurnal warming generate vertical stratification and convective horizontal exchange flows driven by destabilizing buoyancy fluxes that play an important role in the transport of nutrients, pollutants, and chemical substances between the littoral and pelagic regions also modulating nearshore plankton communities [10]. The convectively driven horizontal flows are the result of a density difference in the horizontal direction. Solar radiation during the day leads to warmer water in the shallows than in the adjacent deeper regions, and this developing contrast in temperature between shallow and deep waters produces variations in water density that generate convective water exchange [11] [12]. Likewise, SGD seeps along the shoreline produce density contrast due to freshwater influx. These density-driven buoyant plumes modify nearshore circulation patterns influencing phytoplankton distribution [13].

Despite their important environmental and social consequences, the mechanisms driving phytoplankton variability in nearshore waters and the eventual occurrence and evolution of HABs are difficult to fully understand due to their short timescales of variation (hours) and intrinsic multifactorial nature in which physical, biological, and geochemical processes intervene. High

biomass outbreaks may occur that are too rapid and intense to be explained by reported microalgal cell growth rates [14], suggesting that physical accumulation mechanisms may be major drivers of these events. For example, coastal blooms in the Mediterranean Sea are typically dominated by dinoflagellates showing individual growth rates in the range of 0.4 - 0.8 day^{-1} [16] [15]. However, it is not uncommon for daily cell abundance to vary by more than threefold [17].

Circulation in the nearshore can either favor or hamper high-biomass HAB development by either accumulating or dispersing algal populations. For example, wind-driven circulation has been observed to maintain and generate algal blooms both in the sea and in lakes by downwind transport and accumulation of HAB-producing cells [14] [18] [19]. Likewise, the presence of intense temperature and salinity gradients at sea fronts can represent a boundary favoring phytoplankton accumulation [20] [21] [22]. In the coastal boundary zone, these accumulation mechanisms operate at short timescales (hours). However, their influence on the dynamics of nearshore phytoplankton remains to be fully explored While most field studies on HAB dynamics have focused on mesoscale (kilometers to hundreds of kilometers) or regional processes, much less attention has been paid to fine-scale processes occurring at sub-kilometer spatial resolution and over short timescales (hours). However, these small-scale processes can be critical for understanding the mechanisms underlying rapid biomass accumulation in coastal areas.

Here, we examine the dynamic interplay between the physical forcings that drive the cross-shore displacement of the nearshore water strip and its influence on phytoplankton accumulation at Palma Beach (Balearic Islands) during a small algal biomass outbreak. We focus on the understanding of the diel variability patterns of phytoplankton as determined by wind-forced transport and buoyancy currents. Data from three moorings and repetitive sampling in nearshore waters and a simple advection-diffusion 1D model are used to interpret the retention-dispersion mechanisms regulating the short-term (hours) phytoplankton variability.

2. Methods

2.1. Site description

The case study site, Palma Beach (39°31'11.5" N, 2°44'06.3" E), is located on the inner coast of Palma Bay, southern Mallorca In summer, it features (Balearic Islands), and is characterized by a semi-enclosed morphology with high anthropogenic influence. During the summer, the area exhibits calm hydrodynamic conditions driven by weak sea breeze winds, negligible tidal forcing, minimal wave activity, and a gently sloping bathymetry (∼10 m per km) (10 m per km), which lacks breaker zones and promotes water mass retention (Jordi et al., 2011). This 5 km-long beach is subject to intense human pressure from urban development and seasonal tourism, both of which contribute to environmental stress. A notable feature affecting coastal water quality is the seepage of a nutrient-enriched groundwater from the coastal

aquifer often fuels dinoflagellate blooms [24] along the beach, which introduces elevated levels of dissolved nitrogen and trace elements such as iron into the littoral zone [6][24]. These nutrient inputs create fertile nearshore conditions that, combined with elevated summer sea temperatures, enhance phytoplankton productivity and increase the likelihood of microalgal bloom formation. Such blooms are typically short-lived yet recurrent, occurring from late May through September, and align with seasonal bloom dynamics observed at other Mediterranean coastal sites [17] [43]

2.2. Field data

Temperature, salinity, current velocity, and chlorophyll (θ, S, u, and Chl) were monitored over one week (Julyb 19-25, 2018). Cross-shore transects of near-surface (0.25 m) fluorescence, salinity, and temperature were measured every 3 hours from the shoreline to 600 m offshore using a flow-through system on a small boat [4] (Fig.1). Seawater samples were collected at three points (P1, P6, P9; Fig.1) using 0.6 L Niskin bottles, and chlorophyll concentrations were determined by filtering, allowing fluorescence calibration (see Appendix A.1). Wind (W) data were obtained from an oceanographic buoy 3.5 km offshore (SOCIB). Cross-shore currents were measured with bottom-mounted ADCPs (Nortek HR Aquadopp) attached to poles fixed on the seabed at three locations (M1, M2, M3; Fig. 1), obtaining current profiles from $\sim$0.15 m below the surface to the seafloor every 3 seconds [25].

2.3. A minimal model for the fast nearshore bloom dynamics

To disentangle the mechanisms behind the Chl patterns observed during the field survey, we developed a simple toy model to capture the key environmental processes driving the fast dynamics (on the scale of hours) in the nearshore zone, aiming at minimal parametrization [26]. The phytoplankton standing stock (Chl) is expected to evolve over time due to multiple processes [27]:

$$\frac{\partial Chl}{\partial t} = \text{growth} - \text{grazing} + \text{diffusion}_{x,y,z} + \text{advection}_{x,y,z} - \text{sinking}_{z} \quad (1)$$

where each term acts over different timescales. Reported *in situ* growth rates of dinoflagellates are generally < 1.0 day^{-1} [16], with grazing pressure typically comparable to or lower than this value [28]. To indirectly constrain phytoplankton growth rates during the field survey, we refer to NCP-based estimates from Basterretxea (2024), which reported rates of 0.16-0.25 day^{-1}, indicative of a community not undergoing rapid proliferation. We thus expect growth and grazing to opearate on timescales > 1 day (doubling or halving times). Since the most significant biomass fluctuations in our data occur on the timescale of hours (Fig. 2a), with minimal variance between days and a roughly constant total biomass standing stock throughout the sampling period (-4% daily biomass loss, Fig. 2a, inset), growth and grazing are excluded from the toy model. CTD data reveal vertically homogeneous profiles of θ, S, and Chl (see Appendix Appendix A.2), indicating that wave-driven

turbulence in these shallow waters maintains well-mixed conditions, thereby limiting vertical processes such as sinking or behavioral adaptations (e.g., diel vertical migration). These semplifications are supperted by previous Empirical Orthogonal Function (EOF) analysis conducted on the dataset [25], which found that over 90% of the daily *Chl* variance was driven by variations in environmental factors, particularly cross-shore currents, cross-shore wind, and temperature. Alongshore variations, although necessary to solve the hydrodynamics correctly, are thus also excluded from the toy model.

Overall, we hypothesize that the rapid daily fluctuations ($\sim$ hours) in nearshore biomass are primarily driven by horizontal processes resulting from a dynamical equilibrium between advection and diffusion in the cross-shore direction, with growth and grazing modulating the system on longer timescales ($\geq$1 day). The toy model is finally based on three assumptions:

1. All physical drivers producing advective flows follow a daily periodicity
2. The nearshore flow can be reduced to a 1D water mass being pulled back and forward from/to the shoreline, and still capture the main accumulation-relaxation dynamics
3. Phytoplankton biomass (determined as *Chl*) behaves as a well-mixed passive tracer, excluding relevant cell growth and/or grazing, or behavioural aspects (e.g. dinoflagellates diel vertical migration).

The model's first assumption is supported by field data, which show a clear

daily periodicity in wind W(Fig 2a, blue line), temperature θ and salinity S (Fig 2c-d). Moored instruments confirm a similar periodicity in the current data (Fig. 2b for M1; Fig. A.9 for M2 and M3) and reveal a vertically homogeneous flow. The absence of vertical structures supports the hypothesis of a well-mixed system, as expected in shallow waters where wave-breaking-induced turbulence promotes vertical mixing, with the primary dynamics occurring in the cross-shore direction.

2.4. Building the toy model

The Chl retention-release dynamic along the cross-shore direction is modelled with a one-dimensional advection-diffusion equation:

$$\frac{\partial Chl\ (t,x)}{\partial t} = D\frac{\partial^2 Chl\ (t,x)}{\partial x^2} + u(t,x)\frac{\partial Chl\ (t,x)}{\partial x} \tag{2}$$

where x is the longitudinal direction along the transect, t is time, $u(t,x)$ are the cross-shore currents, and D is an effective diffusion coefficient accounting for the mixing processes in the surf zone [30, 31]. The advective term is expressed as a linear combination of the main environmental forcings acting on the system (wind, salinity and temperature gradients):

$$u(x,t) = u_W(x,t) + u_S(x,t) + u_\theta(x,t) \tag{3}$$

where u_W is the wind-driven flow, u_S is the current component due to the fresher water input along the shoreline, and u_θ is the current driven by cross-

shore temperature gradients. The advective term omits tidal currents, as they are expected to play a negligible role in the system's dynamics (see Appendix A.4 for details).

As shown in Fig 2a, wind at the study site followed a daily cycle, peaking at 5 m/s onshore in the afternoon and dropping and inverting to 2 m/s offshore at night. Assuming a linear relationship between the wind speed W and the advected current $u_W = 5 \cdot 10^{-3} \cdot W$ [19], we expected wind-driven flows ranging from 2.5 cm/s onshore to 1 cm/s offshore.

The horizontal gradients in θ and S create a buoyant flow driven by density differences, where the time required for the flow to develop and its magnitude depend on the steepness of the density gradient. Following [32], we assume that the horizontal current developing in response to a horizontal density gradient $\partial\rho/\partial x$ is given by the unsteady inertia of water:

$$\rho_0 \frac{\partial^2 u}{\partial t \partial z} = g \cdot \frac{\partial \rho}{\partial x} \tag{4}$$

where ρ is the water density, ρ_0 its average value, g the gravity, and z the vertical direction. The effect of thermal and haline expansion on water density can be separated:

$$\frac{\partial p}{\partial x} = \rho_0 \left(\alpha \frac{\partial \theta}{\partial x} + \beta \frac{\partial S}{\partial x} \right) \tag{5}$$

where α and β are the thermal and haline contraction coefficients of seawater.

The field survey monitored $\partial\theta/\partial x$ and $\partial S/\partial x$, allowing us to estimate the expected magnitudes and timing of thermal and salinity currents via scale analysis of equations 4 and 5 (details in Appendix A.5). Nearshore waters exhibited a daily cycle of heating and cooling, and an afternoon salinity drop (Fig. 2c). During daytime, warmer and fresher water accumulates near the coast, with $\theta(x)$ and $S(x)$ decaying exponentially offshore over 100–200 m (Fig 2d). During nighttime cooling, this effect is confined to the nearshore region (Fig 2d). Using the steepest observed gradients, we estimate typical current magnitudes of 2 cm/s, 7 cm/s, and 10 cm/s associated to differential cooling, heating, and the salinity drop, respectively.

The cross-shore diffusion coefficient (D) cannot be directly measured from field observations. In the surf zone, wave breaking enhances cross-shore mixing, increasing diffusion compared to the open ocean [29]. A rough estimate of D can be derived using the wave breaker height (H), wave period (τ), and surf zone width (X) as $D = (H \cdot X)/\tau$ [30]. For the study site, using $H = 0.25$ m, $\tau = 4$ s, and $X = 20$ m [33], we estimate $D = 1.25\ m^2/s$, consistent with reported coastal diffusion values (0.5–1.7 m^2/s) [34], and tested $D = 1.25\ m^2/s$ $\pm 50\%$ variations in the model.

The apparent flow compressibility introduced by the 1D model aligns with the behavior of projected incompressible 3D flows, where dimensionality reduction inherently relaxes mass conservation in omitted directions. The model domain is set to 1 km, with no-flux boundary conditions applied at both ends

to ensure conservation of mass. One boundary represents the coastline; the other, corresponding to open sea, is located far enough to minimize boundary effects. The simulation runs for 7 days to ensure that dynamical equilibrium is reached and that the results are independent of initial conditions. We tested different values of u_θ and u_s within the range provided by the scaling analysis, assuming an offshore exponential decay of the forcing consistently with the gradients that drives them (Fig 2d). The numerical analysis was developed using the FiPy partial differential equation (PDE) solver [35] and is provided in the Appendix A.6.

3. Results

3.1. Coupling between the diel wind pattern and Chl

Field data show that most biomass was concentrated in a dense nearshore stripe a few hundred meters wide. We calculated the total algal biomass contained in this stripe, Chl_{int}, by integrating each Chl transect within 150 meters of the coastline. Averaging Chl_{int} across sampling days revealed a clear diurnal pattern: biomass doubled in the afternoon compared to nighttime and early morning, with the steepest increase from 7:00 AM until a sharp decline at 4:00 PM (Fig 2a). In contrast, when Chl_{int} was calculated over the entire transect and averaged daily, total biomass remained fiarly constant throughout the period (-4% daily biomass loss, Fig 2a inlet), indicating no significant net growth or decline of the total population. This suggests that the observed daily variation in nearshore biomass is driven by

redistribution rather than biological growth. A comparison of the nearshore Chl_{int} ($\leq$ 150 m) with cross-shore wind W revealed a strong temporal correlation between the two timeseries (2a): the onset of morning winds coincided with the steepest biomass increase, while the afternoon wind relaxation coincided with its decline. To explore the time-lagged relationship between the Chl_{int} and W, we calculated their cross-correlation as:

$$\textit{Cross-Corr}\,(\tau) = \frac{\sum(Chl_{int}(t) - \mu_{Chl_{int}}) \cdot (W(t+\tau) - \mu_W)}{N \cdot \sigma_{Chl_{int}} \cdot \sigma_W} \tag{6}$$

where $\mu_{C_{int}}$ and μ_W are the averages of Chl_{int} and W, $\sigma_{Chl_{int}}$, and σ_W are the respective standard deviations, and N the number of points. The cross-correlation pattern reveals a distinct oscillation between positive and negative values, indicating periodic shifts between in-phase and out-of-phase behavior (Fig. 3a). The cross-correlation peaks at $\tau = 0$, suggesting that the rise in onshore winds is closely associated with the immediate accumulation of biomass near the coast. The spectral density of the cross-correlation reveals a clear peak corresponding to a 24-hour period (3b), implying that the two time series remain in phase if one is shifted by 24 hours. We performed a sensitivity analysis varying the integration range of Chl_{int} up to 600 m from the shoreline, and found that synchronization with W extended to approximately 300 m offshore (see Appendix Appendix A.8). Overall, the data suggest that a periodic, wind-driven accumulation mechanism underlies the observed Chl_{int} pattern.

3.2. Diel retention and dispersion pattern

The cross-shore distribution of *Chl* also exhibited a daily pattern (Fig. 4a). In the morning, we observed a shoreward exponential increase in algal biomass, reaching a peak near the shore in the mid-morning, measured at 5 mg/m^3. In the afternoon, the *Chl* distribution flattens and the peak is shifted offshore, relocating between 50 and 100 meters from the coast. This spatial redistribution of the biomass was consistent between different days and suggests the presence of a mechanism producing a horizontal off-shore displacement of the biomass.

The currents measured in M3 (Fig. 2b) also display a well-defined diurnal pattern, aligning with the expected diurnal variability of currents driven by wind advection and cross-shore gradients in temperature and salinity (Fig. 2a, 2c). Onshore currents of $\sim$ 1 cm/s are observed during the night hours and start increasing at 7:00 AM, following the rise of the onshore winds (Fg. 2b). A sharp flow inversion is observed at 1:00 PM as nearshore currents start flowing offshore until 6:00 PM. This flow inversion coincides with the maximum thermal gradient associated with water differential heating. We can expect this offshore flux to be sustained by the salinity decline, peaking between 4:00 and 7:00 PM and also contributing to the offshore flux of the water. Apart from a mild nearshore recirculation cell observed after 6:00 PM, the ADCP data suggests the absence of a clear 2D structure in the proximity of the coast. The current direction remains fairly constant along the verti-

cal, suggesting a mainly 1D displacement of the water column governed by horizontal currents.

Fig. 4a shows the comparison between the cross-shore Chl transects measured during the field campaign and the profiles of the passive tracer distribution resulting from the 1D model at the corresponding time of the day. The best agreement between model and data is found for thermal and haline currents ranging between 1 cm/s and cm/s, coinciding with the range of currents measured by the current meter in M3 (Fig. 2b).The model result is displayed as an average between the different model runs within this optimal thermal and haline current ranges. Figure 4b shows the diurnal variability of Chl_{int} calculated at three different distances from shore (100 m, 300 m, 600 m). Overall, the observed diurnal dynamic of the Chl field is fairly captured by the 1D approximation, both in terms of the cross-shore spatial distribution (4a) and the integrated profile (4b). The model overall captures the dynamics of the nearshore biomass, the agreement between the model and the data decreasing further away from the coastline.

4. Discussion

In the present study, we adopt a simple advection-diffusion model to analyze the short-term dynamics of the biomass contained in the nearshore coastal stripe, treating Chl as a passive, well-mixed tracer. The spatial and temporal resolution considered—sub-kilometer and hourly scales—is rarely

addressed in HAB research, which typically focuses on broader spatial and longer temporal frameworks. Although this approach deliberately simplifies the system by omitting biological variability, it shows high exploratory and conceptual value since it allows us to successfully shed light on the roles of three interacting physical forcings (wind, temperature and salinity) without introducing a high level of complexity and parametrization. Field data were collected during the decline phase of a small algal outbreak, whose multi-day trend (Fig.2a, inlet) and in-situ measured growth rates [25] suggest a biologically quiescent regime. It is unlikely that the inclusion in the model of processes such as growth, mortality, and grazing would alter our results, since they act at larger timescales. Indeed, [36] show that when nutrient supply or light limitation lacks significant spatial variability, circulation and phytoplankton population dynamics are separable: stirring and mixing spatially structure plankton distributions, while biological dynamics govern population size. Here, measured planktonic metabolism (estimated as net community production, NCP per unit Chl) was uniform across the transects [25], suggesting an underlying spatially homogenous light and nutrient field. Given that equation **??** Thus, consistent with [36], we find that cross-shore plankton distribution is controlled by physical processes, whereas the magnitude of the variations depends on phytoplankton standing stocks driven by nutrient availability, temperature, and biotic interactions (e.g., parasites and grazers).

Overall, our approach successfully captures the main dynamics of the bloom and its simplicity allows us to disentangle and isolate key factors. Short-term fluctuations in Chl concentration can be explained by periodic particle retention-dispersal mechanisms driven by the opposing flows induced by wind and density gradients (Fig. 3 and 4). The data indicate that changes in the cross-shore wind speed and in Chl are synchronized up to 300m from the coastline (Fig. 2a and Appendix A.8). The morning rise of the landwards winds is accompanied by a shoreward exponential increase in biomass. Differential heating and freshwater inputs produce a mass of buoyant water, which is retained near the coast by the onshore winds. Temperature and salinity gradient build up during the day, eventually overcoming the wind, leading to offshore dispersal of phytoplankton in the early afternoon. At nighttime, the nearshore flow inverts, possibly due to differential cooling. The model enable us to isolate individual contributions and probe potential scenarios (see Appendix A.11). Our analysis shows that wind is the primary driver of the overall accumulation pattern, with over a 4-fold increase in the model residuals for 50% variation in wind strength (Fig. **??** and Appendix A.11). Likewise, the weakening of buoyant flows generated by temperature gradients expedite the deviation of diel biomass responses, with significant late afternoon variability.

Thermal and haline currents were estimated via scale analysis, providing order-of-magnitude estimates of the expected flows. The observed biomass

variability was successfully reproduced for a range of values within this estimate, with flows between 1 and 4 cm/s, consistent with ADCP measurements. A nighttime low-magnitude onshore flow ($\sim$1 cm/s) was crucial to counteract the afternoon offshore biomass dispersal driven by the thermohaline gradient. This onshore flow, although present in the ADCP measurements, cannot be fully explained by the scale analysis, which predicts an onshore cooling-driven flows only after $\sim$ 4:00 AM (see Appendix Appendix A.5).

The observed physical mechanism of diel retention–dispersion cycles leads to the daily nearshore compression of phytoplankton biomass, potentially intensifying a range of density-dependent processes— such as particle encounters, exudate accumulation, self-shading, and oxygen production or depletion—with significant ecological implications. Increased daytime biomass concentration nearshore can reduce light penetration, limiting growth through self-shading, while also altering oxygen dynamics. The localized accumulation of phytoplankton-derived compounds may create chemical hotspots that influence predator behavior [44] or trigger the emergence from dormancy in parasites [45], and elevated cell densities can increase encounter rates between phytoplankton and their microzooplankton grazers [46], potentially enhancing top-down control and reshaping trophic interactions. In this context, the observed mechanism may not initiate blooms but could contribute to their decline by facilitating predator–prey interactions and amplifying self-regulatory

feedbacks, ultimately influencing bloom persistence and termination.

Real-world processes surely exhibit a greater degree of complexity than cannot be captured by this approximation. At other stages of the bloom, the timescales of biological dynamics may align more closely with those of the physical redistribution mechanisms considered here. During the exponential growth phase, diel gradients in light, nutrients, and temperature can drive differential growth rates between nearshore and offshore waters, overlapping with the proposed daily redistribution dynamic. Similarly, in the termination phase, severe grazing or parasitism might lead to a sharp collapse of the population. Behavioral factors influencing the diurnal vertical positioning of cells within the water column may inhibit their dispersion by currents and alter their horizontal transport [18, 37, 38], rendering the one-dimensional approximation overly simplistic. Likewise, nearshore flows likely has two- and three-dimensional structures. The flow produced by differential heating and cooling is intrinsically not symmetric [32], with water heating stratifying a superficial buoyant plume, while water cooling produces a more turbulent vertically mixed flow. Although the measured nearshore currents do not show clear 2D structures, offshore moored data suggest that the transitional flow between the onshore and offshore circulation patterns is characterized by the formation of two counterrotating convection cells (Fig. 5). This pattern may partially arise from unresolved spatial structures in buoyancy forcing, driven by the collinear interaction between thermal and haline flows

(see Appendix Appendix A.9). Such complexity likely modulates water residence times and affects the timing of biomass redistribution along the transect, contributing to the model–data mismatch observed offshore. These 2D structures cannot be fully characterized with the deployed instrumentation and not included in the model. Other bio-physical processes might also contribute to coastal plankton accumulation, such as the amplification of the thermally driven circulation by the bloom itself through increased water light absorption [39, 40].

Despite these limitations, the model offers valuable insights into the key mechanisms driving phytoplankton variability and provides a framework for understanding its transport in the nearshore zone, a key factor in coastal ecosystem management. The results presented herein reveal how competing physical forces drive the accumulation/dispersion of nearshore phytoplankton. The model's ability to reproduce observed patterns underscores its value in interpreting data of beach water quality, and its simplicity allows for application to other passive tracers dispersed in nearshore waters such as municipal discharges, microplastics, or the distribution and fate of eggs and larvae from littoral organisms.

Acknowledgments

This research was supported by funding from the European Union's H2020 programme under the Marie Skłodowska-Curie grant agreement No. 955910,

as well as projects DIACOM (PID2022-143018NB-I00) and HABSYS (TED2021-132886B-I00 PRTR) funded by the Ministerio de Ciencia, Innovación y Universidades (MICINN), the Agencia Estatal de Investigación (AEI), and the Fondo Europeo de Desarrollo Regional (FEDER, UE). The work was carried out within the framework of the activities of the Spanish Government through the "María de Maeztu Centre of Excellence" accreditation awarded to IMEDEA.

Author contributions

G. Basterretxea: Conceptualization, Funding acquisition, Methodology, Writing – review and editing. **I. Tuval**: Conceptualization, Funding acquisition, Methodology, Supervision, Writing – review and editing. **M. Zanoli**: Methodology, Formal analysis, Writing – original draft.

Variable names, symbols, units	
Chl	Chlorophyll $[mg/m^3]$
Chl_{int}	Integrated Chlorophyll $[mg]$
x	Cross-shore direction $[m]$
t	Time $[s]$
D	Cross-shore diffusion coefficient $[m^2/\mathrm{s}]$
θ	Seawater temperature $[^\circ C]$
S	Seawater salinity [PSU]
W	Cross-shore wind [m/s]
u	Total cross-shore advection current $[m/s]$
u_s	Salinity driven advection current $[m/s]$
u_θ	Temperature driven advection current $[m/s]$
u_W	Wind driven advection current $[m/s]$
α	Seawater thermal expansion coefficient $[1/K]$
β	Seawater haline expansion coefficient $[1/PSU]$
τ	Wave period $[1/s]$
H	Wave breaker height [m]
X	Surf zone width $[m]$
ρ	Water density $[kg/m^3]$
ρ_0	Average water density $[kg/m^3]$
z	Water depth $[m]$
g	Gravitational constant $[m/s^2]$

Table 1: List of used abbreviations, symbols and units

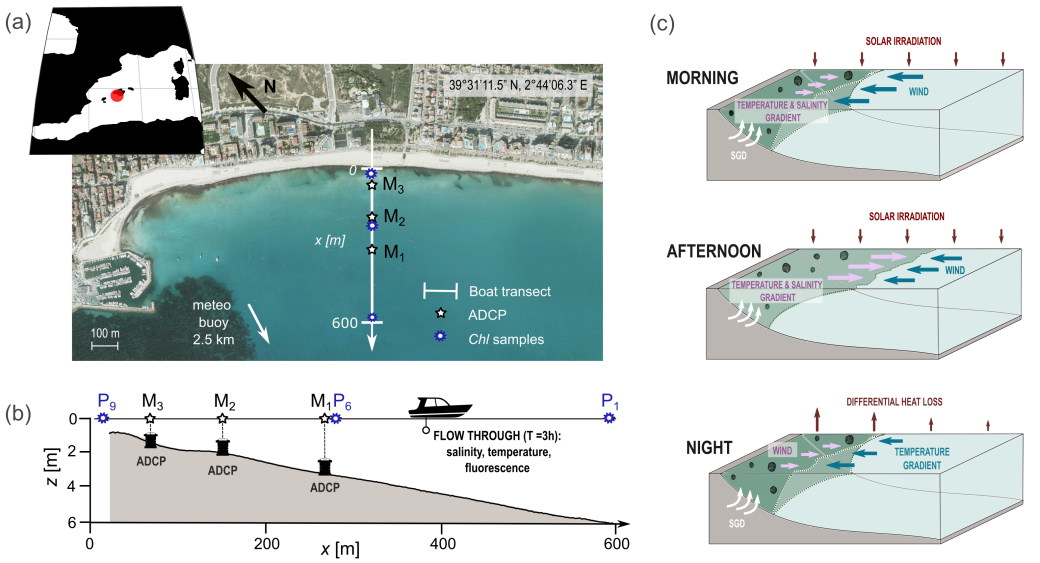

Figure 1: **(a):** Sampling site in Palma Beach, Mallorca, Spain. The cross-shore transect travelled by the sampling boat is shown in white and sets the x-coordinate of the analysis. The position of the Acoustic Doppler Current Profiler (ADCP) moorings (M1, M2, M3) and the *Chl* sampling points (P1, P6, P9) are marked on the transect line. **(b):** Beach bathymetry along the transect **(c):** Schematics of the natural forcings acting on the system at different times of the day. During daytime, the onshore sea-breeze forcing competes with an off-shore buoyant flow driven by the differential heating of the water and coastal SGD. During the night, the winds weaken and reverse, while differential cooling of the water drives an on-shore flow.

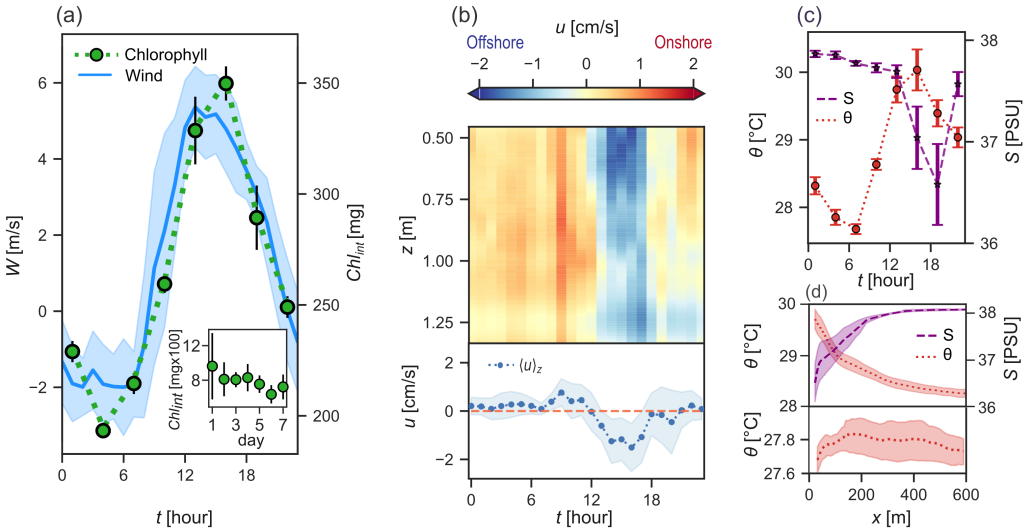

Figure 2: **(a)**: Hourly averages of cross-shore winds and total biomass accumulated near the shoreline Chl_{int} ($<$ 150 m) during the 6-day sampling period (excluding data from storm day on 22/07/2018). Chl_{int} ([mg]) is obtained by integrating Chl concentration profiles ([mg/m^3]) along the transect direction and depth profile, assuming a homogeneous distribution of Chl along the water column. Inset: daily Chl_{int} average calculated over the entire transect (<600 m). **(b)** Typical daily patterns of the cross-shore currents from ADCP data measured at M3 (top), and its vertical average along z (bottom). The typical current for each hour is calculated by averaging the currents measured at that specific hour across all days of the sampling period. The entire water column flows cohesively in one direction with no clear recirculation cells developing near the shore, suggesting a mainly 1D flow. Currents shown in the bottom panel are obtained as the vertical average of those shown in the top panel. **(c)** Typical values of water temperature and salinity near the shoreline (25 m) at different hours of the day. The typical temperature and salinity for each hour is calculated by averaging the temperature and salinity measured at that specific hour across all days of the sampling period. **(d)** Temperature and salinity profiles from the shoreline to 600 m at the times showing the strongest cross-shore gradients. Up: temperature profile associated to differential heating at 1:00 PM (red dotted line), salinity profile during the salinity drop at 19:00 PM (dashed violet line). Down: temperature profile associated to differential cooling at 07:00 AM.

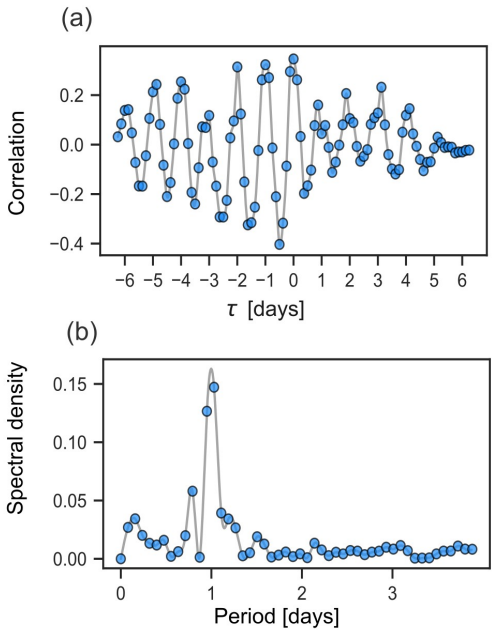

Figure 3: **(a)** Cross-Correlation between Cross-Shore Wind and Chl_{int} (<150 m) Timeseries. The cross-correlation is calculated on the mean-subtracted timeseries. The maximum correlation is found at zero lag, and successive maximum positive values are observed every 24 hours, suggesting that variations in nearshore *Chl* are synchronized with variations in the cross-shore wind. **(b)** Spectral density of the Fourier transform of the cross-correlation in Panel B. A clear peak at a 1-day periodicity is observed.

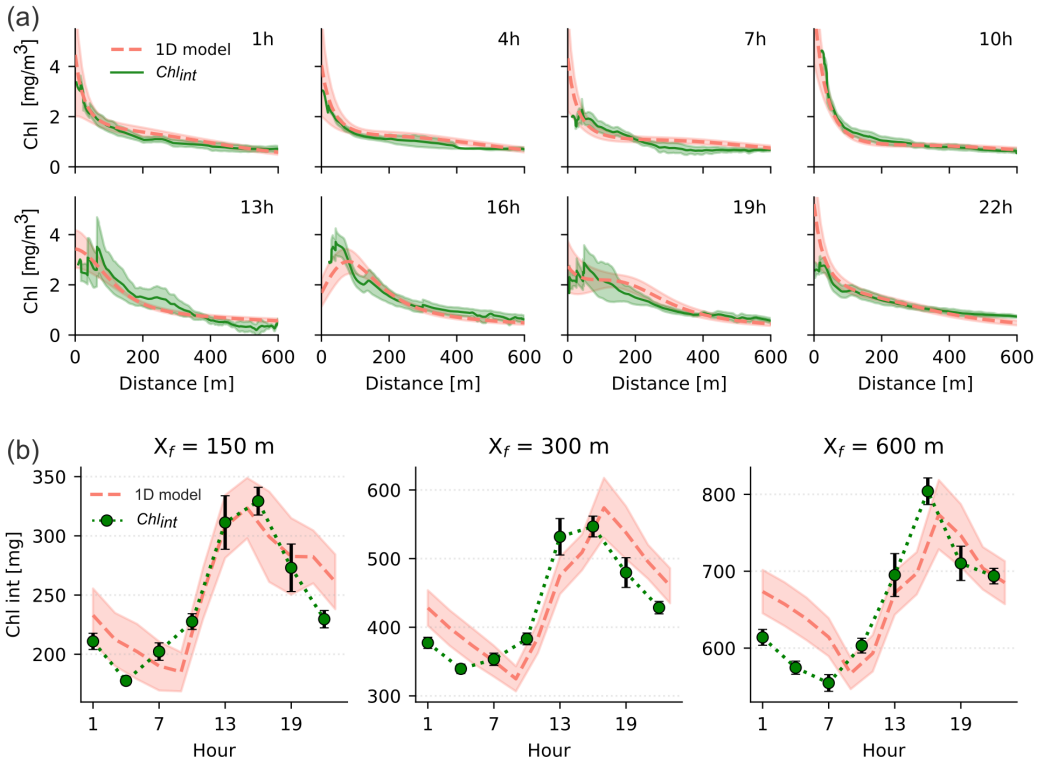

Figure 4: **(a)** Cross-shore transects of *Chl* biomass [mg/m^3], averaged at the same hour across all days of the sampling period (green line). The pink line shows the biomass accumulation predicted by the 1D model as a result of the dynamical equilibrium between the forcings resulting from the wind and the thermal-haline syphon. The model output is represented as the ensemble mean of all simulations across the range of diffusivities and advection flows explored (dashed line), restricting the ensemble to a thermal heating flow $u_\theta > -4$ cm/s. The number in parentheses represents the average daily residual between observed and modeled *Chl* concentrations at matching transect locations for the best-performing model run, expressed in mg/m^3 **(b)** Chl_{int} of a typical day at 150m, 300m and 600m from the coast (green dots) obtained integrating the *Chl* profiles in panel a. The pink dashed line marks the model ensemble mean, and the shaded area its standard deviation.

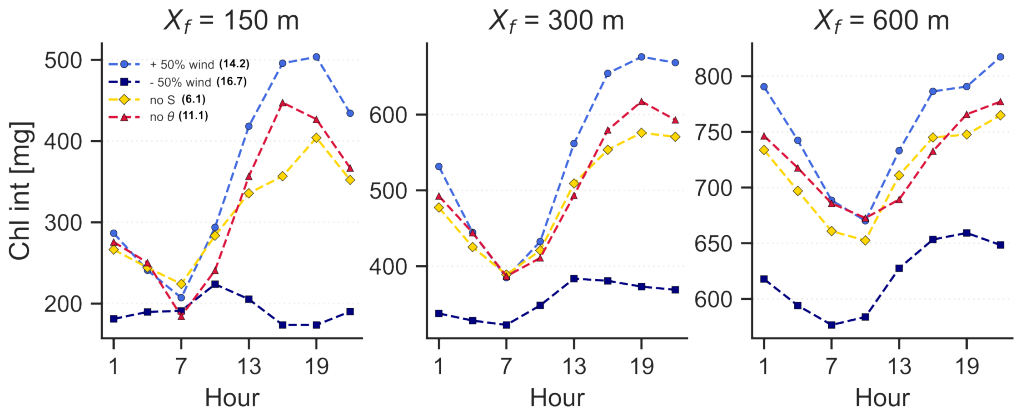

Figure 5: Integrated profiles of average cross-shore transects of *Chl* biomass [mg] up to three different distances from the coast (150, 300 and 600 m), compared with that modelled in 4 alternative scenarios: +50% and -50% wind, no salinity-driven flow and no temperature-driven flow. The number in parentheses represents the average daily residual between observed and modeled chlorophyll concentrations at matching transect locations of each model run, expressed in mg Chl/m^3

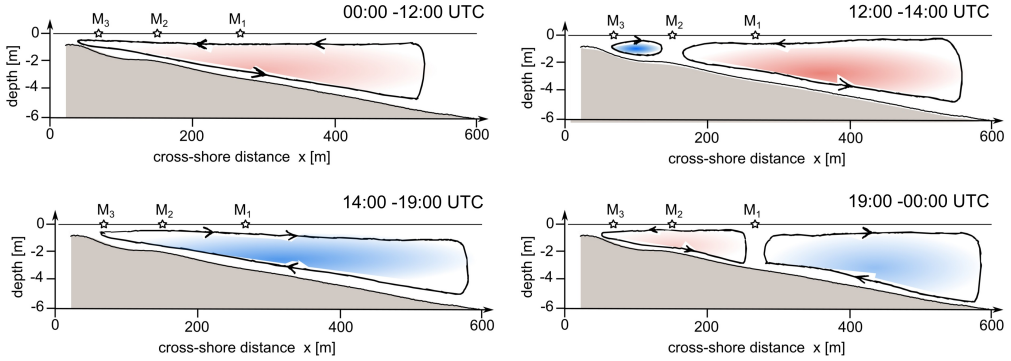

Figure 6: Current data from moored instrumentation in M1,M2,M3 suggests that the transitions between the morning onshore flow and the afternoon offshore flow are characterised by the formation of two counter-rotating convection cells. In both cases, the transition flow starts close the coastline and gradually extends seawards. The onshore morning flow, driven by winds and differential cooling of the water, is counteracted by the kick in of a thermo-haline syphon, the buoyant water flowing offshore. After sunset, differential cooling of the littoral waters promts the shorewards flow.

References

[1] J. H. Landsberg *The Effects of Harmful Algal Blooms on Aquatic Organisms*, Reviews in Fisheries Science, 10:2, pp. 113-390, 2002

[2] E. Berdalet, A. S. Pavaux, R. Abós-Herràndiz, et al., *Environmental, human health and socioeconomic impacts of Ostreopsis spp. Blooms in the NW Mediterranean*, Harmful Algae, Elsevier, vol. 119, 102320, 2022.

[3] E. Berdalet, M.A. McManus, O.N. Ross, et al., *Understanding harmful algae in stratified systems: Review of progress and future directions*, Deep Sea Research Part II: Topical Studies in Oceanography, vol. 101, pp. 4-20, 2014

[4] G. Basterretxea, F. J. Torres-Serra, E. Alacid E, et al., *Cross-Shore Environmental Gradients in the Western Mediterranean Coast and Their Influence on Nearshore Phytoplankton Communities. Front. Mar. Sci.* 5:78. 2018

[5] H. W. Paerl, *Coastal eutrophication and harmful algal blooms: Importance of atmospheric deposition and groundwater as "new" nitrogen and other nutrient sources*, Limnology and Oceanography, Wiley Online Library, vol. 42, no. 5part2, pp. 1154–1165, 1997.

[6] G. Basterretxea, A. Tovar-Sanchez, A.J. Beck, et al., *Submarine Groundwater Discharge to the Coastal Environment of a Mediterranean*

Island (Majorca, Spain): Ecosystem and Biogeochemical Significance, Ecosystems, Springer Link, vol. 13, no. 15, pp. 629–643, 2010.

[7] C. Enriquez, I. Mariño-Tapia, G. Jeronimo, et al., *Thermohaline processes in a tropical coastal zone*, ontinental Shelf Research, vol. 69, pp. 101-109, 2013

[8] Y. R. Rao and D. J. Schwab, Transport and mixing between the coastal and offshore waters in the Great Lakes: a review , Journal of Great Lakes Research, Elsevier, vol. 33, no. 1, pp. 202–218, 2007.

[9] F. J. Tapia, J. Pineda, F. J. Ocampo-Torres, et al., *High-frequency observations of wind-forced onshore transport at a coastal site in Baja California*, Continental Shelf Research, Elsevier, vol. 24, no. 13–14, pp. 1573–1585, 2004.

[10] J. Sturman, C. Oldham and G. Ivey, *Steady convective exchange flows down slopes*, Aquatic Sciences, Springer, vol. 61, no. 3, pp. 260–278, 1999.

[11] D. E. Farrow and J.C. Patterson, *On the response of a reservoir sidearm to diurnal heating and cooling. Journal of Fluid Mechanics.* vol. 246, pp. 143-161, 1993

[12] A. Ghane and L. Boegman, Turnover in a small Canadian shield lake. Limnology And Oceanography. **66**, 3356-3373 (2021)

[13] M. A. McManus and C. B. Woodson, Plankton distribution and ocean dispersal, Journal of Experimental Biology, The Company of Biologists Ltd, vol. 215, no. 6, pp. 1008 -1016, 2012.

[14] R. P. Stumpf, R. W. Litaker, L. Lanerolle, et al., *Hydrodynamic accumulation of Karenia off the west coast of Florida*, Continental Shelf Research, Elsevier, vol. 28, no. 1, pp. 189–213, 2008.

[15] S. L. Strom and T. A. Morello, *Comparative growth rates and yields of ciliates and heterotrophic dinoflagellates*, Journal of Plankton Research, Oxford University Press, vol. 20, no. 3, pp. 571–584, 1998.

[16] W. Stolte and E. Garcés, *Ecological Aspects of Harmful Algal In Situ Population Growth Rates*, in *Ecology of Harmful Algae*, E. Granéli and J. T. Turner, Eds., Berlin, Heidelberg: Springer Berlin Heidelberg, 2006, pp. 139–152. doi: 10.1007/978-3-540-32210-8_11.

[17] G. Basterretxea, E. Garcés, A. Jordi, et al., *Modulation of nearshore harmful algal blooms by in situ growth rate and water renewal*, Marine Ecology Progress Series, Inter-Research, vol. 352, pp. 53–65, 2007.

[18] G. Basterretxea, E. Garcés, A. Jordi, et al., *Breeze conditions as a favoring mechanism of Alexandrium taylori blooms at a Mediterranean beach*, Estuarine, Coastal and Shelf Science, Elsevier, vol. 62, no. 1, pp. 1–12, 2005.

[19] J. H. G. Verhagen, *Modeling phytoplankton patchiness under the influence of wind-driven currents in lake*, Limnology and Oceanography, American Society of Limnology and Oceanography, vol. 39, no. 7, pp. 1551–1565, 1994.

[20] J.H. Simpson, D.J. Edelsten, A. Edwards, et al., *The Islay front: Physical structure and phytoplankton distribution*, Estuarine and Coastal Marine Science, Elsevier, vol. 9, no. 6, pp. 713–IN1, 1979.

[21] H.H. Seliger, K.R. McKinley, W.H. Biggley, et al., *Phytoplankton patchiness and frontal regions*, Marine Biology, Springer, vol. 61, pp. 119–131, 1981.

[22] R. Pingree, P. Pugh, P. Holligan, et al., *Summer phytoplankton blooms and red tides along tidal fronts in the approaches to the English Channel*, Nature, Nature Publishing Group, vol. 258, pp. 672–677, 1975.

[23] A. Jordi, G. Basterretxea and D.P. Wang, *Local versus remote wind effects on the coastal circulation of a microtidal bay in the Mediterranean Sea*, Journal of Marine Systems, Elsevier, vol. 88, no. 2, pp. 312–322, 2011.

[24] V. Rodellas, J. Garcia-Orellana, A. Tovar-Sánchez, et al., *Submarine groundwater discharge as a source of nutrients and trace metals in a Mediterranean bay (Palma Beach, Balearic Islands)*, Marine Chemistry,

[25] G. Basterretxea, J. S. Font-Muñoz, M. Kane, et al., *Pulsed wind-driven control of phytoplankton biomass at a groundwater-enriched nearshore environment*, Science of the Total Environment, vol. 955, pp. 177123, 2024.

[26] A. J. Jakeman, S. Elsawah, H.-H. Wang, S. H. Hamilton, L. Melsen and V. Grimm, Towards normalizing good practice across the whole modeling cycle: its instrumentation and future research topics, Socio-Environmental Systems Modelling, vol. 6, pp. 18755, 2024.

[27] B.W. Frost, *The role of grazing in nutrient-rich areas of the open sea, Limnology and Oceanography*, Limnology and Oceanography, vol. 36, no.8, pp. 1616–1630, 1991.

[28] A. Gutiérrez-Rodríguez, M. Latasa, R. Scharek, R. Massana, G. Vila, and J. M. Gasol, *Growth and grazing rate dynamics of major phytoplankton groups in an oligotrophic coastal site*, *Estuarine, Coastal and Shelf Science*, vol. 95, no. 1, pp. 77–87, Nov. 2011. doi: 10.1016/j.ecss.2011.08.008.

[29] J. M. Restrepo, S. C. Venkataramani and C. Dawson, *Nearshore sticky waters*, Ocean Modelling, Elsevier, vol. 80, pp. 49–58, 2014.

[30] D.L. Inman, R.J. Tait and C.E. Nordstrom, *Mixing in the surf zone*, Journal of Geophysical Research, American Geophysical Union, vol. 76, no. 15, pp. 3493–3514, 1971.

[31] G. Savidge, *Studies of the effects of small-scale turbulence on phytoplankton*, Journal of the Marine Biological Association of the United Kingdom, Cambridge University Press, vol. 61, no. 2, pp. 477–488, 1981.

[32] S. G. Monismith, J. Imberger and M. L. Morison, *Convective motions in the sidearm of a small reservoir*, Limnology and Oceanography, Wiley Online Library, vol. 35, no. 8, pp. 1676–1702, 1990.

[33] L. Gómez-Pujol, A. Orfila, B. Cañellas, et al., *Morphodynamic classification of sandy beaches in low energetic marine environment*, Marine Geology, Elsevier, vol. 242, no. 4, pp. 235–246, 2007.

[34] M. S. Spydell, F. Feddersen and R.T. Guza, *Observations of drifter dispersion in the surfzone: The effect of sheared alongshore currents*, Journal of Geophysical Research: Oceans, American Geophysical Union, vol. 114, no. C7, pp. 1–14, 2009.

[35] J. E. Guyer, D. Wheeler and J. A. Warren, *FiPy: Partial Differential Equations with Python*, Computing in Science & Engineering 11(3) pp. 6-15 (2009), doi:10.1109/MCSE.2009.52

[36] M. A. Srokosz, A. P. Martin and M. J. Fasham, *On the role of biological dynamics in plankton patchiness at the mesoscale: An example from the eastern North Atlantic Ocean*, Journal of Marine Research, vol. 61, no. 4. 2003.

[37] A. G. Fujimura, J. H. M. Reniers, C. B. Paris, et al., *Mechanisms of Cross-Shore Transport and Spatial Variability of Phytoplankton on a Rip-Channeled Beach*, Frontiers in Marine Science, Frontiers, vol. 5, pp. 183, 2018.

[38] R. D. Hetland, D. J. McGillicuddy and R. P. Signell, *Cross-frontal entrainment of plankton into a buoyant plume: The frog tongue mechanism*, Journal of Marine Research, vol. 60, 2002.

[39] M. Kahru, J.M. Leppanen and O. Rud, *Cyanobacterial blooms cause heating of the sea surface*, Marine Ecology Progress Series, Inter-Research Science Center, vol. 101, no. 1/2, pp. 1–7, 1993.

[40] A. M. Edwards, D. G. Wright and T. Platt, *Biological heating effect of a band of phytoplankton*, Journal of Marine Systems, Elsevier, vol. 49, no. 1, pp. 89–103, 2004.

[41] D.E. Farrow and J.C. Patterson, *On the stability of the near shore waters of a lake when subject to solar heating*, International Journal of Heat and Mass Transfer, Elsevier, vol. 36, no. 1, pp. 89–100, 1993.

[42] Y. Mao, C. Lei and J. C. Patterson, *Unsteady near-shore natural convection induced by surface cooling*, Journal of Fluid Mechanics, Cambridge University Press, vol. 642, pp. 213–233, 2010.

[43] A. Regaudie-De-Gioux, L. Latorre and G. Basterretxea, *Phytoplankton metabolism in a stratified nearshore ecosystem with recurrent harmful*

algal blooms (HABs), Journal of Plankton Research, Oxford University Press, vol. 45, no. 6, pp. 785–793, 2023.

[44] Q. Güell-Bujons, M. Zanoli, I. Tuval, A. Calbet and R. Simó, Distinctive chemotactic responses of three marine herbivore protists to DMSP and related compounds, The ISME Journal, Oxford University Press, vol. 18, no. 1, p. wrae130, 2024.

[45] E. Garcés, E. Alacid, A. Reñé, K. Petrou and R. Simó, Host-released dimethylsulphide activates the dinoflagellate parasitoid Parvilucifera sinerae, The ISME Journal, Oxford University Press, vol. 7, no. 5, pp. 1065–1068, 2013.

[46] A. W. Visser and T. Kiørboe, Plankton motility patterns and encounter rates, Oecologia, Springer, vol. 148, pp. 538–546, 2006.

Appendix A. Appendix

Appendix A.1. Transects calibration: from fluorescence to Chl concentration

Water fluorescence was measured using an Enviro-T in-line fluorometer along the transects shown in Fig.1 of the manuscript, serving as a proxy for microalgae biomass as described in [4]. For each transect, water samples were collected at three points (P1, P6, and P9 in Fig. 1), and Chl concentration was measured by filtration.

Detritus and debris, such as suspended leaf fragments, can become lodged in the fluorometer and interfere with sensor readings, causing anomalies—peaks if the debris is fluorescent or valleys if it is non-fluorescent. To remove these artifacts, all fluorescence data were post-processed using a Python routine. Major peaks and valleys in the signal were identified, fitted to a Gaussian model, and removed. The gap in the signal was filled by linear interpolation and the reconstructed signal was smoothed with a third-order Savitzky–Golay polynomial filter, which reduces noise while preserving the primary signal pattern.

Fluorescence readings were converted to Chl concentrations using water samples for calibration. Since the fluorescence signal depended on instrument conditions at the time of measurement (e.g., battery level), a three-point calibration was performed for each transect individually. A linear relationship was assumed between the instantaneous fluorescence (Flu) and Chl concen-

tration. For a transect measured at time t_0:

$$Flu(x, t_0) = a(t_0) \cdot Chl(x, t_0) + b(t_0) \tag{A.1}$$

where $a(t)$ and $b(t)$ are specific to each individual transect and are obtained performing a linear fit between the Chl point values in P1,P6,P9 and the corresponing measured values of Flu at the same locations. Fig. A.7 illustrates the agreement between point chlorophyll measurements and their corresponding calibrated estimates across three sampling stations.

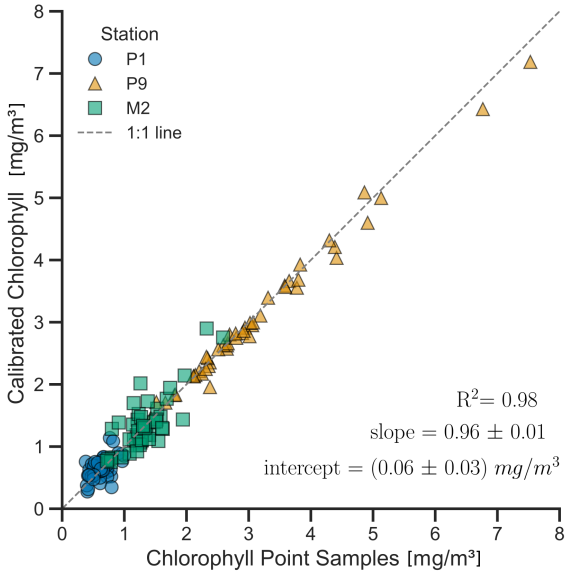

Figure A.7: Comparison between point chlorophyll measurements (mgm^{-3}) and corresponding chlorophyll estimates from the calibration. Data from the three stations are shown: P1 (circles), P9 (triangles), and M2 (squares). The dashed line indicates the 1:1 relationship. Close alignment of points with the line suggests good agreement between observed and calibrated values across all stations.

Appendix A.2. CTD vertical profiles

To assess the vertical structure of the water column during sampling, CTD profiles of temperature, salinity, and chlorophyll fluorescence were collected at multiple stations on 20 July 2018 (Fig. A.8). These profiles reveal vertically homogeneous distributions across all measured parameters within the 0–7 m depth range, indicating well-mixed conditions throughout the sampled layer. While data from the uppermost 0.5 m of the water column are unavailable—where surface accumulation of larger cells could potentially occur—the lack of thermal or haline stratification below this skin layer, combined with the absence of subsurface chlorophyll maxima or phytoplankton aggregations, further supports the inference of vertical homogeneity in these shallow coastal waters.

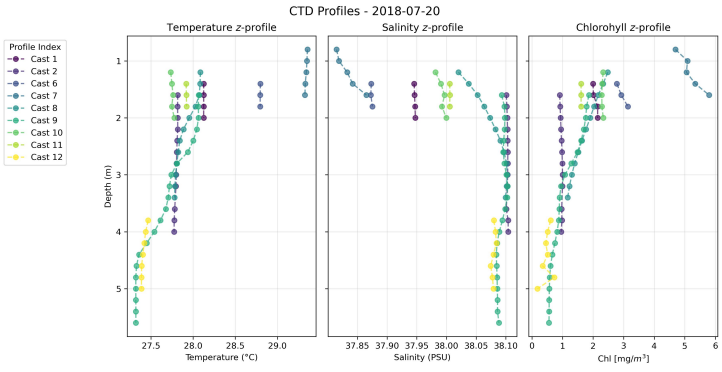

Figure A.8: CTD vertical profiles collected on 20 July 2018 at multiple stations along the transects. Each panel shows measurements as a function of depth of: (left) temperature ($\hat{c}irc$C), (middle) salinity (PSU), and (right) chlorophyll-a concentration (mg/m^3).

Appendix A.3. ACDP profiles in M1, M2, M3

FigureA.9 displays the currents measured by the ACDP during the field survey at three transect locations (M1, M2, and M3), placed at 70 m, 150 m, 280 m from the coastline. For each hour of the day, the current vertical profile is calculated by averaging the currents measured at that specific hour across all days of the sampling period. These profiles, therefore, represent the typical daily current patterns at the study site. Overall, the current direction appear consistent along the vertical direction down to a depth of 1–1.5 meters, indicating that the flow is predominantly one-dimensional within this layer. Notably, the offshore flow observed at M3 in the early afternoon (between 1 PM and 7 PM) weakens significantly at M2 and re-emerges at M1 with a two-hour delay (between 3 PM and 9 PM). The nighttime onshore flow, which is weaker at M3, reaches speeds of up to 2 cm/s at M2 and M1. This onshore flow can only be partially attributed to the differential cooling of nearshore waters compared to the open sea and is introduced into the model as a phenomenological current. Although the mechanisms driving this flow are not fully explained by the "thermal siphon" effect, the model suggests that the presence of this flow is essential to counterbalance the afternoon flushing of biomass and accurately reproduce the observed daily biomass pattern.

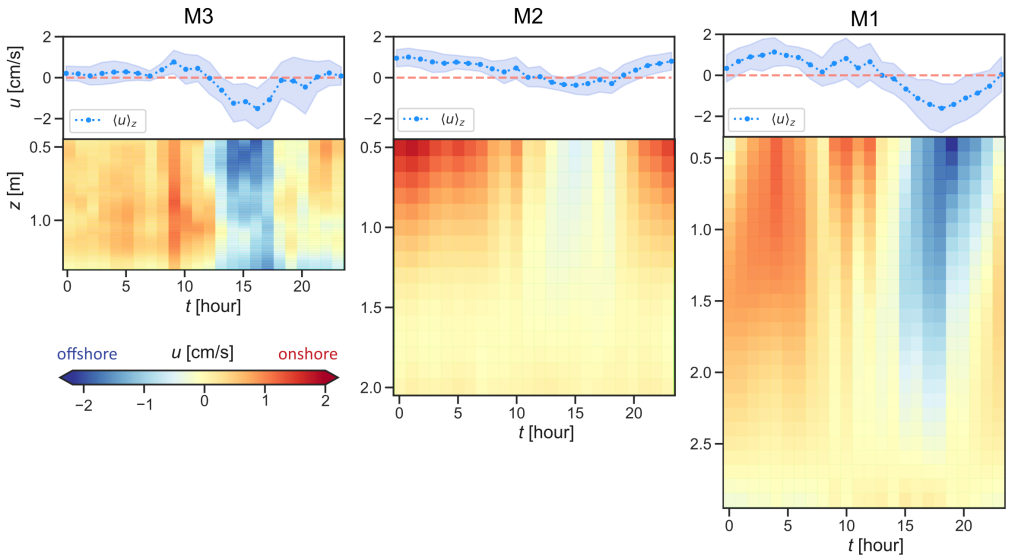

Figure A.9: ACDP data in M3 (70 m), M2 (150 m), M1 (280 m) measured during the field survey. Each colormap represents the vertical profile of the flow obtained averaging the current data measured at the same hour of the day across different days. The upper plots represent the vertical average of the flows depicted in the colormaps. Onshore flows are represented in red and offshore flows in blue.

Appendix A.4. Tidal contribution to the advective term

Tidal forcing was not explicitly isolated in our analysis. However, tidal contributions — though relatively weak in magnitude (0.7–1.3 cm/s)— could compete with the other forcings, particularly during nighttime hours when wind diminishes. To estimate the potential influence of tides on the proposed retention–dispersion mechanism, we compared sea level data recorded at station M3, the closest point to the shoreline, with ADCP measurements of total currents, which integrate all physical forcings. The left panel of Fig. A.10 shows sea level (SL) at M3 during the field survey, while the right panel

presents an hourly averaged SL profile constructed in the same manner as the "typical day" used for other model variables (e.g., wind, temperature, salinity). Although tidal cycles do not follow a strict 24-hour cycle, this averaging provides a first-order approximation of their diel influence. Notably, the tidal signal appears roughly in anti-phase with the observed diel current patterns: ebb tide (falling sea level in the morning) would typically drive offshore flow, and flood tide (rising sea level in the afternoon) would promote onshore flow. In contrast, ACDP measurements show the reverse —onshore flow in the morning and offshore flow in the afternoon—indicating that the diel current signal is not primarily tidal in origin. It is likely, instead, that tidal currents partially dampen the net circulation driven by diel forcing. This suggests that the retention–dispersion dynamics described in the main text may be even more pronounced in the absence of tidal modulation.

Appendix A.5. Scale analysis of the temperature and salinity driven currents

The advective currents generated by density gradients, which arise from cross-shore variations in temperature and salinity, are estimated through scale analysis. This approach provides the expected order of magnitude for the flows driven by these gradients. If we consider a fluid system initially in an equilibrium flow to which a reversed temperature gradient is suddenly applied, the system will try to restore stability through a convective motion. This stabilizing convection is governed by the unsteady inertia of the

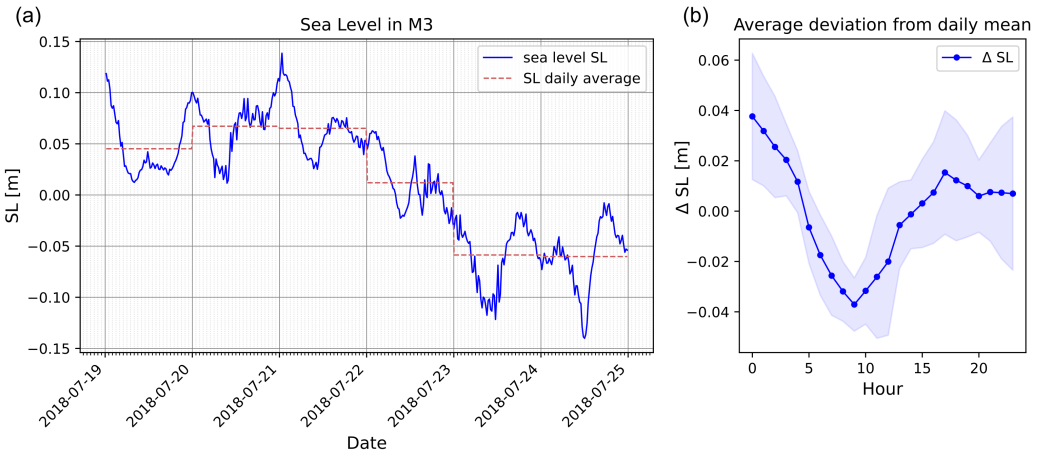

Figure A.10: (a): Sea level (SL) time series during the field survey as measured in M3. The red dotted line is the daily mean of the sea level. (b) Average hourly sea level deviation relative to daily mean (SL). For each day, SL was calculated relative to that day's mean value. These hourly deviations were then averaged across all days to represent the typical daily cycle of sea level fluctuations.

water:

$$\rho_0 \frac{\partial^2 u}{\partial t \partial z} = g \cdot \frac{\partial \rho}{\partial x} \tag{A.2}$$

where u is the cross-shore current, ρ_0 is the average density of the water, g the gravity, and x, z and t are the cross-shore horizontal direction, the vertical direction, and time respectively. We assume that density gradient due to thermal expansion and the one due to haline expansion can be separated:

$$\frac{\partial \rho}{\partial x} = \rho_0 \left(\alpha \frac{\partial \theta}{\partial x} + \beta \frac{\partial S}{\partial x} \right) \tag{A.3}$$

where α is the thermal contraction coefficient of seawater, and β the haline contraction coefficient.

Following Monismith 1990[32], the scale analysis on equations A.2 and A.3 provides an estimate of the expected magnitudes for the thermal and salinity currents U_θ and U_S, together with the typical spin-up timescales T_θ and T_S for such currents to develop from an initial state of rest:

$$U_\theta = \sqrt{g \cdot \alpha \cdot \Delta\theta \cdot L_z^\theta} \qquad U_S = \sqrt{g \cdot \beta \cdot \Delta S \cdot L_z^S} \tag{A.4}$$

and:

$$T_\theta = \frac{U_\theta \cdot L_x^\theta}{g \cdot \alpha \cdot \Delta\theta \cdot L_z} \qquad T_S = \frac{U_S \cdot L_x^S}{g \cdot \beta \cdot \Delta S \cdot L_z} \tag{A.5}$$

where L_x^θ and L_x^S are the typical horizontal scales of the temperature and salinity gradients, and L_z is the typical scale of the system in the vertical direction.

Typical values for the steepness of the gradients $\Delta\theta/L_x^\theta$ and $\Delta S/L_x^S$ are estimated from the temperature and salinity fields $\theta(x,t)$ and $S(x,t)$ measured during the field campaign (figure 2, panel B). We use $L_z = 1$ m as vertical scale of the system. This vertical estimate is extracted from the ACDP current profiles, which show that the currents flow cohesively within the first 1 m layer (Fig. A.9). As horizontal scales, we use $L_x = 600$ m for flows driven by thermal heating and salinity drop. For thermal cooling, we use $L_x = 200$ m, as the morning thermal inversion does not extend throughout the transect, but is restricted to the nearshore band (Fig. A.13a-b). We consider a typical temperature variation of $\Delta\theta = 1.5$ °C for differential heating, $\Delta\theta =$

0.1 °C for differential cooling, and $\Delta S = 1$ PSU for the salinity drop. This parameters result in a thermal afternoon offshore current of $U_\theta = 7$ cm/s with spin up time $T_\theta = 3$ h, in a haline current of $U_S = 10$ cm/s with spin up time $T_S = 1.5$ h and a morning onshore thermal current of $U_\theta = 2$ cm/s with spin up time $T_\theta = 3$ h.

In our approximation, we assume the buoyancy flows to act on time windows centered in the moments of steepest temperature and salinity gradients (refer to Fig. A.13b-d). We assume the steepest gradients to appear at 7:00 AM (differential cooling), 2:30 PM (differential heating) and 5:30 PM (salinity drop). For the latter two, the chosen time corresponds to the central value between the sampling times when maximum temperature and salinity gradients where measured.

We assume that the system required a time T_θ and T_S to reach the flows U_θ and U_S at 7:00 AM, 2:30 PM and 5:30 PM for the flows driven by differential cooling, differential heating and the salinity drop respectively. We assume that, symmetrically, the "spin-down" time for the system to stop flowing after the disappearance of the density gradient will be approximately the same as the timescale of the spin-up time, as we expect the slowing down of the system to be governed by the same physical processes as the spin-up. We thus define the buoyancy currents to act within a time window twice the typical spin-up timescale, centered around the moments of maximum gradients. This corresponds to differential cooling acting between 4 AM and

10 AM, differential heating between 11:30 AM and 5:30 PM, and the salinity forcing to act between 4:00 PM and 6:30 PM.

The flows predicted by the scale analysis overall match in terms of timing and directions with the ones measured by the ACDP at the location closest to the shore (M3). The scaling predicts an offshore flow driven by buoyancy flows between 11:30 AM and 6:30 PM, coinciding with the measured flows (see Fig. A.9), partially counterbalanced by the onshore wind-driven flows. The onset of the winds at 7:00 AM together with the action of flows driven by differential cooling between 4 AM and 10 AM matches well with the increase of the onshore flow measured in M3 at 7:00 AM. The scale analysis cannot explain the onshore flow measured throughout the full night hours, which is introduced in the model as a phenomenological current between 9:00 PM and 4:00 AM.

Appendix A.6. Codes of the 1D model

The 1D advection-diffusion equation is implemented using the FiPy partial differential equation (PDE) solver. The code developed is available at the git repository `https://gitlab.com/medeazanoli/1d_advection_diffusion_wind_thermo-haline_syphon.git`

Appendix A.7. Bloom decline

We calculated the total nearshore chlorophyll by integrating the measured *Chl* field across the entire transect (600 m). Figure A.11 shows the temporal

evolution of total algal biomass throughout the sampling period. The data suggest that the system was near saturation, with biomass entering a phase of gradual decline. A linear fit to the data indicates that total biomass decreased at a rate of -36 ± 11 mg/ day^{-1}, corresponding to an average daily loss of approximately 4% relative to the initial chlorophyll concentration.

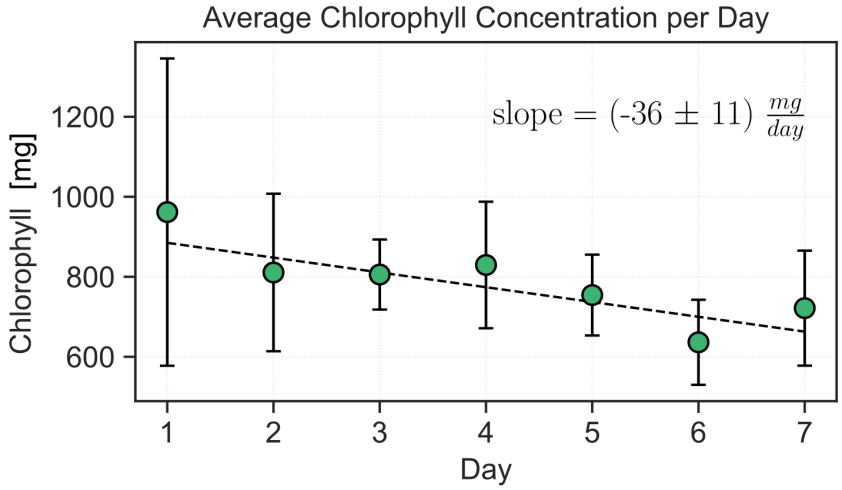

Figure A.11: Mean chlorophyll contained in the transect (600 m) measured over seven days. The dashed black line denotes the best linear fit to the data, with slope ($-36 \pm 11\, mg/\,\mathrm{day}^{-1}$).

Appendix A.8. Sensitivity analysis of the cross correlation between Chl and wind

In section 3.1 of the Results, we explored the time-lagged relationship between the cross-shore winds and the *Chl* biomass accumulated in the nearshore stripe, and found that the two time-series are synchronized between each other. The nearshore stripe was defined to extend between $X_i = 25$ m and $X_f = 150$ m, where $[X_i,\ X_f]$ represents the integration interval. The lower

limit $X_i = 25$ m is set by a practical constraint of the sampling, as the vessel could not approach closer to the coastline. Thus, 25 m is the closest distance at which there is enough fluorescence data to calculate a *Chl* average for each transect. To check that the cross-correlation result is robust, we varied the value of X_f between 80 m and 590 m and recalculated the cross correlation for each value of X_f. Fig. A.12a shows the cross-correlation for different values of X_f, and A.12b the time lag τ in equation 6 of the manuscript resulting in the maximum correlation. We find that the nearshore biomass stripe is homogeneously synchronized with the cross-shore winds up to X_f = 310 m.

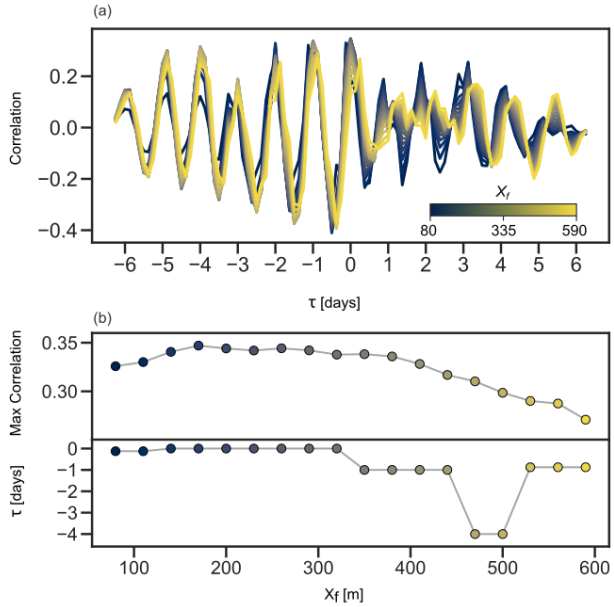

Figure A.12: **(a)** Cross-Correlation between Cross-Shore Wind and *Chl* Timeseries for different values of the biomass integration range X_f, from $X_f = 80$ m (dark blue line) to $X_f = 590$ m (yellow line) **(b)** The maximum correlation obtained for each tested value of X_f (up), and the corresponding lag τ in days (down).

Appendix A.9. Temperature and salinity cross-shore transects

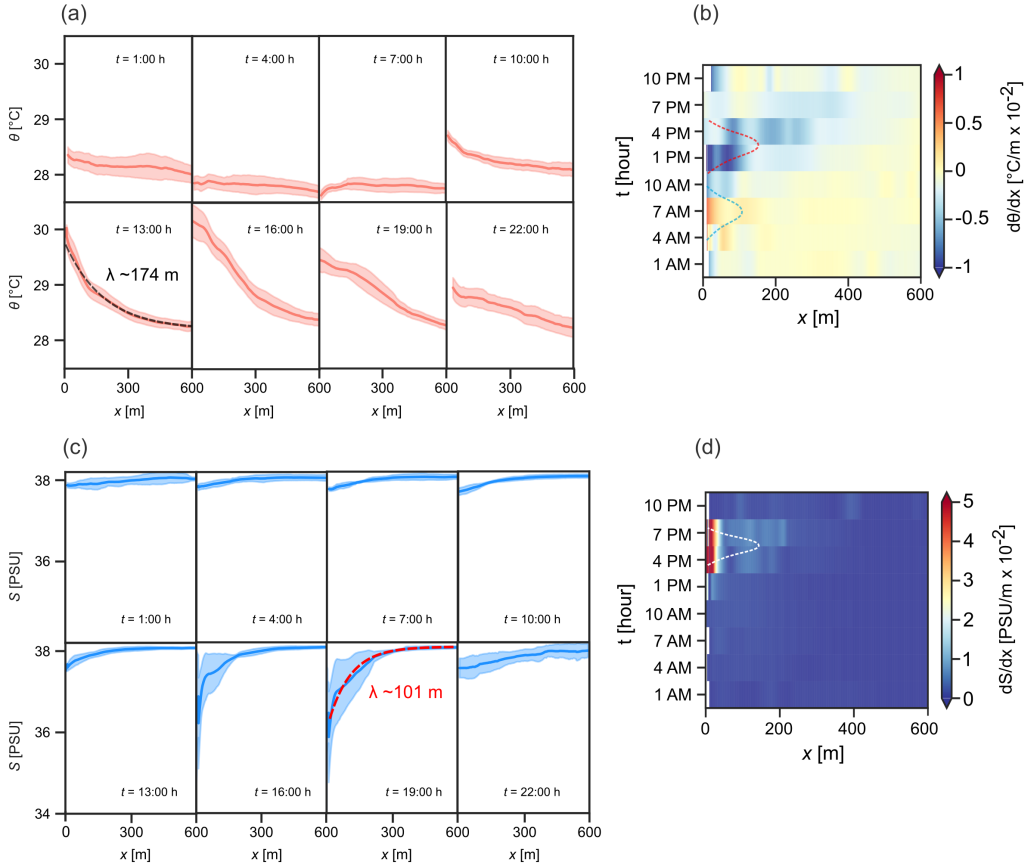

Figure A.13: Cross-shore transects of temperature (a) and salinity (b), averaged across different sampling days. The dashed lines represent the best fit to an exponential function for the temperature profile at 1:00 PM and the salinity profile at 7:00 PM, when the steepest gradients are observed. The reported value of λ is the constant of the exponential fit. The colormaps on the right show the cross-shore temperature (b) and salinity (d) gradients across the transects shown in (a) and (c) respectively. The derivative in x is calculated from the spline interpolation of each transect.The dotted Gaussian lines indicate the time windows during which buoyancy-driven flows are introduced into the 1D model (in (b): differential cooling marked by the blue line centered at 7:00 AM; differential heating by the red line centred at 2:30 PM. in (d): salinity drop marked by the white line centered at 5:30 PM).

Fig. A.13 shows the temperature and salinity cross-shore transects measured during the field campaign. The transects in Fig. A.13a-c represent the

typical daily cycle of temperature and salinity in the nearshore zone. These are obtained by averaging the transects measured at the same hour across different days of the field survey. The daily evolution of temperature and salinity gradients is consistent across the sampling days, revealing a clear diurnal cycle in the nearshore waters.

The temperature difference between the nearshore waters and the open sea reaches approximately 2 °C during the day, with the steepest gradient observed at 1 PM. At this time, the temperature profile increases exponentially toward the shore, characterized by an exponential decay constant of $\lambda \sim 174$ m. In the afternoon, the temperature gradient relaxes as the nearshore waters cool more rapidly, and the steepest gradient shifts offshore. By the end of the cooling phase, around 7:00 AM, a mild thermal inversion occurs, with the nearshore waters being approximately 0.2 °C colder than the open sea.

The salinity cycle is similarly consistent across sampling days. A sharp salinity drop of 2 PSU is observed between 4 PM and 7 PM, when salinity decreases exponentially towards the shore ($\lambda \sim 101$ m). Fig. A.13b-d shows the cross-shore gradients of temperature and salinity obtained via spline interpolation of the profiles in Fig. A.13a-c. The dotted lines indicate the time windows during which buoyancy-driven currents are implemented in the 1D model. In the model, differential cooling drives an onshore flow from 4:00 to 10:00 AM, peaking around the maximum cooling at 7:00 AM. The differen-

tial heating window is centered at 2:30 PM, spanning from 11:30 AM to 5:30 PM. The salinity-driven flow is active between 4:00 PM and 7:00 PM.

In the model, thermal and haline buoyancy flows are treated independently. However, their overlapping time windows can lead to collinear interactions, introducing more complex patterns. The onset of the haline flow may flush warmer waters offshore with potentially strong velocities (up to 10 cm/s, based on a scale analysis of the steepest observed haline gradient), but its influence remains spatially confined ($\lambda \sim 100$ m; Fig. A.13). The combined effect of these collinear flows could advect warmer waters seaward, displacing the peak thermal gradient offshore. This partial dependency between buoyancy forcings may contribute to the late-afternoon recirculation cell observed in Fig. 6: onshore wind forcing—strongest where land–sea temperature gradients are sharpest—may counteract offshore buoyancy flows nearshore. Beyond ∼200 m, the thermal flow sustained by the warm water offshore advection could dominate, generating a two-dimensional flow structure that modulates water residence times and influences the timing of biomass redistribution across the transect.

Appendix A.10. Sensitivity analysis of the 1D model

The 1D advection-diffusion model was run for different magnitudes of advective currents associated to the thermal (u_θ) and haline flows (u_S), with the addition of a nighttime onshore phenomenological current u^* which is oberved in the ACDP data. For the morning flow driven by differential cool-

ing, we explored current values between 1 cm/s and 4 cm/s between 4:00 AM and 10:00 AM. For the differential heating and salinity-driven flows, we explored current values between 1 cm/s and 8 cm/s, between 11:30 AM and 5:30 PM, and between 4:00 PM and 6:30 PM respectively. The presence of an additional phenomenological onshore current u^* is explored after u_S dissipates (between 9:00 PM and 4:00 AM). A range of magnitudes for u^* is explored between 0 cm/s (no current) and 4 cm/s as for the flow driven by differential cooling. The model was run with all combinations of these parameters with the three explored values of cross-shore diffusivities D = 1.25 m^2/s, D = 0.675 m^2/s and D = 1.875 m^2/s. For each model run, we calculate the residuals between the biomass data and the distribution of the modelled passive tracer along each individual transect. Averaging the residuals across all eight daily transects gives a single mean value of residual for each model run. Fig. A.14 shows the value of the mean residual for each of the explored parameters combination.

Finally, we explored the following combinations of advective flows:

- u_S : -1 cm/s, -2, cm/s, -4, cm/s, -8 cm/s (λ = 120 m)
- $u_\theta^{onshore}$: 1 cm/s, 2, cm/s, 4 (λ = 100 m)
- $u_\theta^{offhore}$: -1 cm/s, -2, cm/s, -3 cm/s, -4, cm/s, -8 cm/s (λ = 200 m)
- u^* : 1 cm/s, 2, cm/s, 4 cm/s (λ = 100 m)

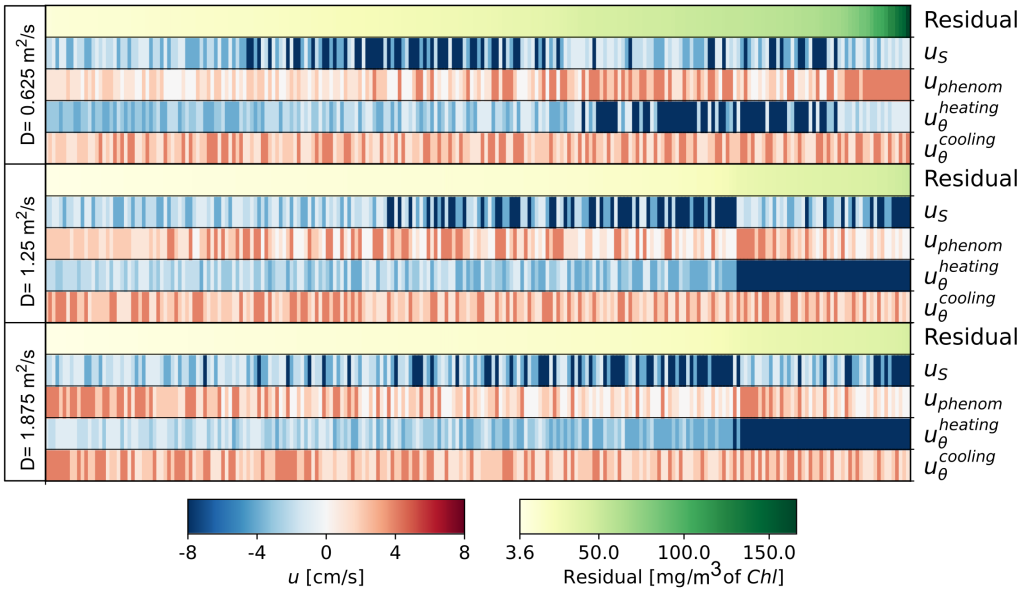

Figure A.14: Residual in mg/m^3 of Chlorophyll between the biomass cross-shore profiles measured during the survey and the profiles obtained in the model for each tested combination of advective fluxes ($u_\theta^{onshore}$, $u_\theta^{offshore}$, u_S and u^*). For each model run, the total residual is as an average of the residuals calculated individually across each transect. Model runs are divided per each tested value of diffusion coefficient D, and ordered from the combination with the lowest residual (left) to the ones with the highest residuals (right). The magnitude of each advective flux is represented by color, red corresponding to onshore fluxes and blue to offshore fluxes.

The model performs on average better for the two higher values of cross-shore diffusivities. The best agreement between modelled and measured biomass distribution is found for the intermediate value of cross-shore diffusivity D $= 1.25\ m^2/s$, together with the following magnitudes of advective forcings: $u_\theta^{onshore}$ = 2 cm/s, $u_\theta^{offshore}$= -2 cm/s, u_S= -2 cm/s and u^*= 2 cm/s. The modelled cross-shore distribution for this set of parameters is shown in Fig. A.15.

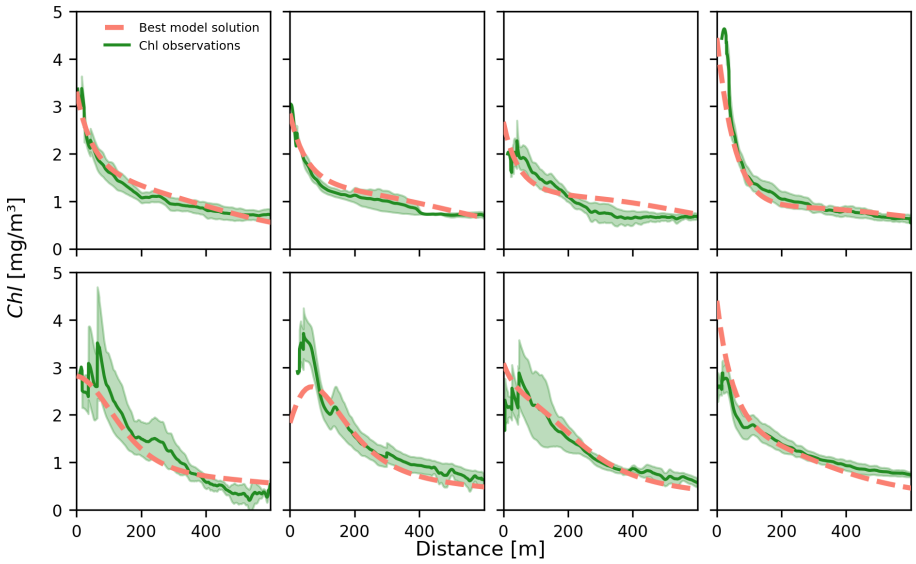

Figure A.15: Comparison between observed and modelled cross-shore biomass distribution for the set of parameters corresponding to the lowest residual ($D = 1.25\ m^2/s$, $|u_\theta^{onshore}| = |u_\theta^{offshore}| = |u^*| = 2\ cm/s$, $|u_S| = 2\ cm/s$)

Appendix A.11. Alternative scenarios: exploration of the individual role of the physical forcings

The model predicts that the daily patterns observed in the biomass distribution emerge from the dynamical interplay between physical forcings of different origin (wind, temperature and salinity gradients). We can thus investigate how the increase, the weakening or the disappearance of these forcings would affect the biomass pattern. To do so, we considered the set of parameters that best fit the field data ($D = 1.25\ m^2/s$, $|u_\theta^{onshore}| = |u_\theta^{offshore}| = |u^*| = 2\ cm/s$, $|u_S| = 1\ cm/s$) and modified individually the contribution of each forcing, except for the phenomenological current u^* which is left unchanged. We considered the following modifications of the forcings: an increase and

decrease by a 50% of the wind strength, and the selective disappearance of either the temperature or the salinity driven flows.

The exploration of these alternative scenarios highlights the critical role of wind in counteracting biomass dispersion driven by buoyancy flows. A 50% reduction in wind strength leads to a pronounced afternoon flush of biomass, effectively halving the total biomass retained within the most nearshore stripe (Fig.**??**a-b). Conversely, increasing the wind strength by 50% doubles the biomass accumulation in the same region. Further offshore, the impact of wind on total biomass fluctuations diminishes. This is consistent with the expectation that buoyant flows weaken exponentially with distance from the coastline, as their driving gradients operate over a scale of only a few hundred meters (Fig.A.13). As a result, beyond this nearshore region, biomass modulation becomes increasingly independent of buoyancy-driven flows, and the wind's counterbalancing influence becomes less significant.

Overall, our findings demonstrate that wind is the primary driver of the observed biomass accumulation patterns, with its strength modulating the amplitude of daily biomass variations. Selectively eliminating one of the two buoyancy-driven flows (Fig. **??**c-d) introduces deviations in the afternoon biomass variability relative to the observed data. In the case of the temperature driven flow, we can appreciate the role of the differential cooling flow in mantaining the biomass accumulation in the nearshore zone in the early morning (7:00 AM, Fig.A.13. Salinity gradients, on the other hand, play a

887 more marginal role in modulating the physico-biological interaction of this
888 particular system, where the salinity driven flow kicks in with a few hours
889 delay with respect to the one driven by differential heating.

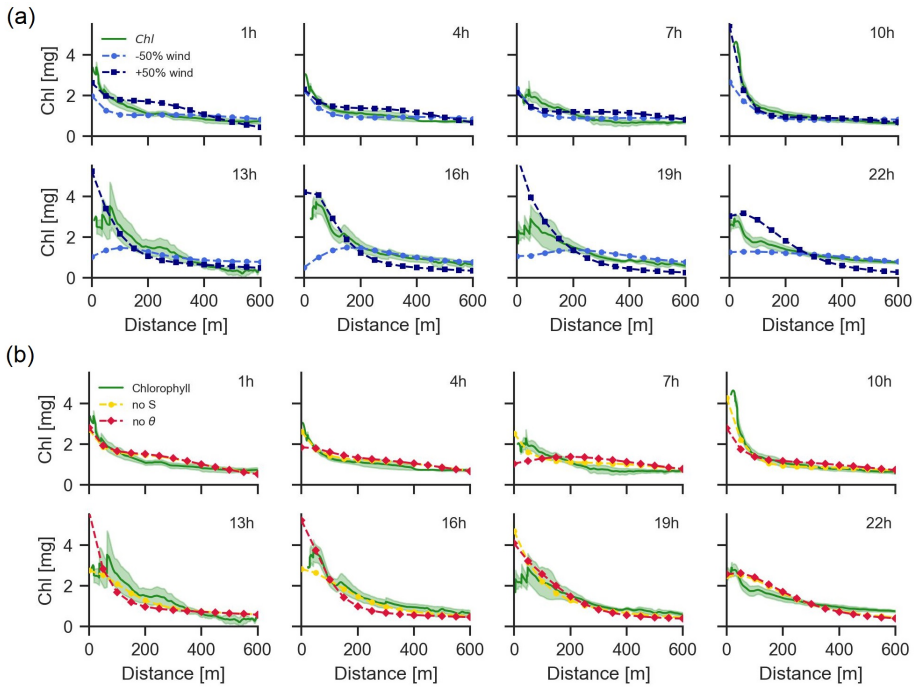

Figure A.16: